DIRECT SELECTIVE LASER SINTERING OF TOOL STEEL POWDERS TO HIGH DENSITY. PART A: EFFECTS OF LASER BEAM WIDTH AND SCAN STRATEGY

C. Hauser, T.H.C. Childs, C.M. Taylor and M. Badrossamay
School Of Mechanical Engineering, University of Leeds, UK

S. Akhtar, C.S. Wright and M. Youseffi
Engineering Materials Research Group, University of Bradford, Bradford, UK

J. Xie, P. Fox and W. O'Neill
Department of Engineering, University of Liverpool, UK

ABSTRACT

This paper describes progress on the Direct Selective Laser Sintering of M2 and H13 tool steel powders, comparing this with previous and further observations on stainless steel powders. The distinguishing feature is the melting of single tracks and layers in deep powder beds. The paper focuses on changing characteristics of the melt pool (mass, volume, aspect ratio, stability) and laser-powder interactivity as the laser beam width, power and scan speed change. It also compares the melt pool of neighbouring tracks during single layer construction. Simulations from a computer model to predict melt pool shape and dimension show reasonable agreement with experimental results at low scan speeds (0.5mm/s). But unexpected increases in melt depth above 1.0mm/s have been observed, suggesting higher values and more variability in laser absorptivity than expected, even approaching 1.0 for the CO_2 laser radiation used in this work.

INTRODUCTION

Selective melting of a metal alloy powder bed, aimed at direct production of one-off components and series tooling, is currently at the forefront of Selective Laser Sintering (SLS) research activities. Recent advances have used specially blended alloys [1] and commercially available powders, including stainless steels [2-4] and tools steels [5,6]. However, reported part densities produced from these powders varies considerably, from just above the tap density of the virgin powder [4,6] to densities exceeding 99% of theoretical density [2,3]. Research in [4] has highlighted that understanding the behavioural differences and dimensional variations of the melt pool and rastering melt front as laser powers and scan speeds change allows for process refinement leading to improvements in the quality of melted layers. This paper extends [4] by also investigating the effects of laser beam width and powder material and how this information might be used to improve the quality of multiple layer components. The microstructure and density of tracks, layers and multiple layers produced in this work are examined in Part B [7].

Running in parallel with the experimental activity is the continual development of a thermally-based finite element model which simulates the SLS process, being the subject of previous papers [8-10]. In this work the model has been used to generate plots of melt track cross-sections which are compared, geometrically, with similar images obtained from the experimental results. It is this comparison between simulation and experiment which leads to conclusions of highly variable absorptivity in the powder beds.

THE FINITE ELEMENT MODEL AND ITS MATERIAL ASSUMPTIONS

The finite element thermal, powder melting and densification model has been described before, both in its 2-D [8,9] and 3-D [10] versions. It has been well-validated experimentally and quantitatively for the SLS of polymers [8,9]. For metals there are more severe issues of selecting correct material data than there are for polymers, when it comes to comparing simulations with experimental data, because of the larger temperature range to which the powder is exposed during processing, the larger difference between the powder bed and solid metal thermal conductivity and, particularly with the use of CO_2 laser radiation, the lower and possibly more variable absorption of the radiation into the bed. In this paper handbook sources have been used for a metal solid's variation of thermal conductivity K and specific heat C with temperature, over the range 20°C to 800°C. A linear variation has been fitted and assumed to apply up to the melting temperature of the metal. With T as absolute temperature

$$K = K_o + K_v T; \quad C = C_o + C_v T \tag{1}$$

Latent heats of melting, L, have been obtained by a rule of mixtures from the latent heats of the alloys' constituent elements. The conductivity K_p and absorptivity α of powder beds at room temperature have been calculated from experiments in which the surface of a bed was exposed to incident non-scanning radiation for a short period of time and the subsequent sub-surface temperature variation in the bed measured by thermocouples. The variation with depth of time for maximum temperature to occur was used to calculate the bed's thermal diffusivity - and K_p obtained from knowledge of the bed's density and material specific heat, and α was obtained from the variation of maximum temperature rise with depth, both in the same theoretical way as described and used in [11]. K_p is assumed to vary with temperature in the same way as K.

Estimates of track size, based on α measured as just described, in many conditions grossly underestimate experimental observations, as will be seen later. Measured track mass per unit length, m_L, has been used to obtain an alternative estimate of absorptivity, α^*. Equation 2 as an equality is an expression for the minimum value of α^*, based on a heat balance. $\alpha^*(P/U)$ is the absorbed energy per unit track length, with P the laser power and U the scan speed while $m_L[C_{av.}(Tm - To) + L]$ is the energy to melt unit track length, where $C_{av.}$ is the average specific heat from ambient bed temperature T_o to the metal's melting temperature Tm.

$$\alpha^* \geq \left[m_L/(P/U)\right]\left[C_{av.}\left(T_M - T_o\right) + L\right] \tag{2}$$

EXPERIMENTATION

Materials. Three types of gas atomised powder have been used in this investigation: M2 (1C-4.15Cr-6.4W-5Mo-2V-bal.Fe) and H13 (0.4C-5Cr-1.3Mo-1.05V-bal.Fe) tool steels and 314S HC stainless steel (0.4C-20Ni-25Cr-1Si-bal.Fe). All powders were obtained from Osprey Metals Ltd, UK and were supplied with a particle size distribution of -150 + 75μm. No heat treatments, additives or fluxes or powder pre-heating was used in this work. A particle size distribution of -75 + 38μm was also investigated for examination in Part B [7] of this paper.

Equipment. SLS was performed in a research machine (Figure 1). A 250W continuous wave CO_2 laser beam with a spot diameter adjustable between 0.55mm and 1.1mm at the focal length was scanned by galvanometer controlled mirrors on to the powder surface inside a controlled environment process chamber. A window in the chamber roof allowed the beam to enter. In the sealed chamber there were two build areas. For multiple layer experiments the build area (70mm in diameter) was at the base of the chamber and on top of the piston assembly which could be moved up and down to control layer depth (accurate to 0.001mm). For single track and layer experiments the build tray (120mm x 150mm x 5mm deep) was used to maximise productivity. A hopper, driven by a stepper motor, deposited and spread fresh powder layers in one operation.

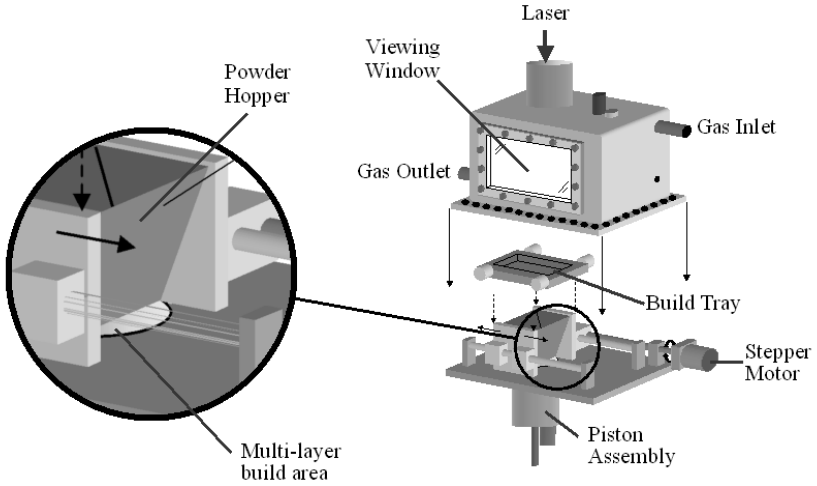

Figure 1. Controlled environment process chamber.

Melting Experiments. All experiments were carried out in an argon environment (obtained from 99.9% purity bottled argon). The chamber was evacuated to a rough vacuum followed by a one minute purge back to atmospheric pressure. This procedure was repeated twice before being followed by a 15 minute pre-sinter purge. During processing the flow rate of argon through the chamber was 3 litres/min and the net pressure was kept at 30mbar above current atmospheric pressure to ensure no air leakage into the chamber. Melting of all powder was carried out in a deep powder layer with a minimum first layer depth of 5.0mm. All scanning conditions for single tracks, layers and multiple layers are reported in Table 1. The experimental conditions were the same for all three powders and two beam widths of 0.55 and 1.1mm were used. The length of the single tracks was nominally 30mm, the size of the layers was nominally 15mm x 12mm and the multiple layers consisted of 12 and 25 layers. The multi-layer results will be reported elsewhere, some in Part B [7].

Table 1: Experimental Conditions.

Experiment	**Laser Power (W)**	**Scan Speed (mm/s)**	**Scan Spacing (% of beam width)**	**Layer Thickness (mm)**
Single tracks	32, 58, 77, 110, 143, 170	0.5, 1 - 12	n/a	n/a
Single Layer	58, 77, 110, 143	0.5, 1, 3, 5, 8, 10	25, 50, 100	n/a
Multiple layers	143	5, 8, 10	25, 50	0.4

Simulations. Simulations of the single track experiments were carried out for all three powder materials. Results for a power of 77W, a beam diameter of 1.1 mm and for scan speeds (mm/s) of 0.5, 1, 2, 4 and 8 are presented here. Material properties used are given in the results section. GSharp V3.1 (AVS Inc) was used to produce 2D sectional views of modelled tracks, with a superimposed grid for dimensional analysis. Image-Pro Plus V4 (Media Cybernetics) was used to evaluate the cross sectional solid area and take measurements from the images.

Further Experiments. Measurements of powder bed diffusivity and absorptivity in the manner of [11] were carried out in air, with a CO_2 laser beam of power up to 10W, defocused to a diameter of 4 mm at the powder bed surface. For these experiments, powder to a depth of 30 mm was placed in a cylindrical container of diameter 60 mm, with a thermocouple placed 10 mm beneath the surface coaxially with the laser beam.

Video and series of still photographs were taken of single tracks as they formed, to gain insight into powder movement during processing. These were taken through the viewing window (Figure 1) using a hand-held digital camera behind a MIG welding glass viewing filter.

RESULTS

Process Maps. Single track process maps that detail heating and melting behaviour of the metal powders as scan speed and laser power change were produced first to highlight areas where the melt pool remained continuous i.e. did not fragment or ball. A fragmented melt pool has been shown in [4] to reduce the surface quality and density of layers. Process maps for M2 and H13 are given in Part B [7]. Figure 2 is for the 314S powder processed using a spot size of 1.1mm. The map is a refinement of the same process map originally presented in [12]. It shows several different qualitative regimes, common to all maps including those from different laser beam diameters. These are regions of continuous flattened tracks, continuous rounded tracks, melted and balled tracks, not fully melted and unmelted regions. Continuous tracks were removed from the bed and sectioned. Observations from all three powders, from P = 50 to 150 W and scan speeds up to 10 mm/s are considered in more detail next.

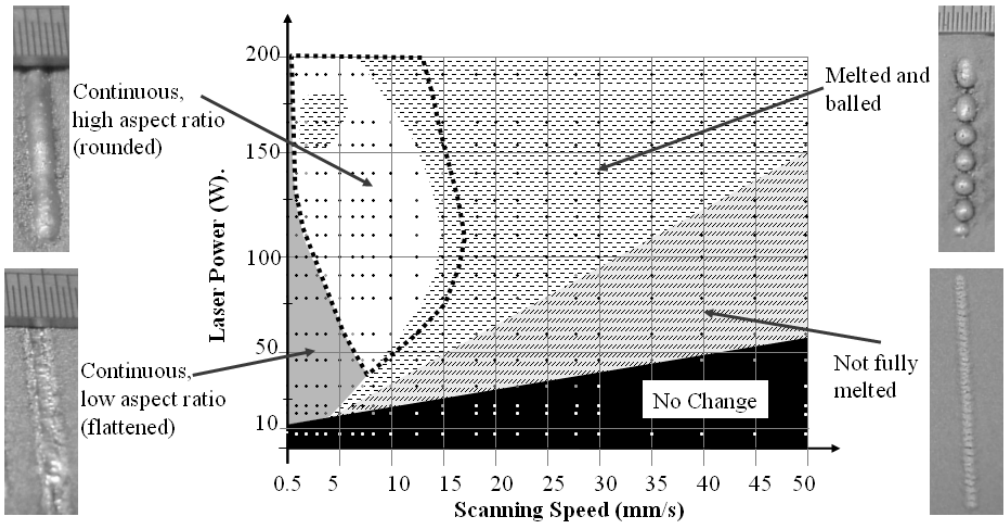

Figure 2. 314S single track process map produced using a laser spot size of 1.1mm.

Track cross-section observations. Figure 3 shows track cross-sections for all three powders at powers of 77, 110 and 143 W. The boundary between the flattened and rounded tracks is added as the solid line. It is noticeable that track cross-section area increases with increasing scan speed as that boundary is crossed. The rounded tracks all have a much larger area than expected from the level of power absorption deduced from the embedded thermocouple tests to measure that (see later). Some qualitative observations may be relevant to this. In the rounded track regime (the whole of the region enclosed by the dashed line in Figure 2), the tracks sink well into the powder bed. Powder to either side of a track collapses into it, leaving a trench surrounding the track. At low scan speeds (~1-2mm/s - Figure 3) track profiles are quite rounded, with only a few groups of satellite particles visible around the lower fringe of the solidified track. However, at higher speeds there are large clusters of sintered bonded particles at the lower surface, giving rise to 'bell' shaped track cross sections. Perhaps these differences arise from the time available for metal in the melt to flow - longer at low than higher scan speeds.

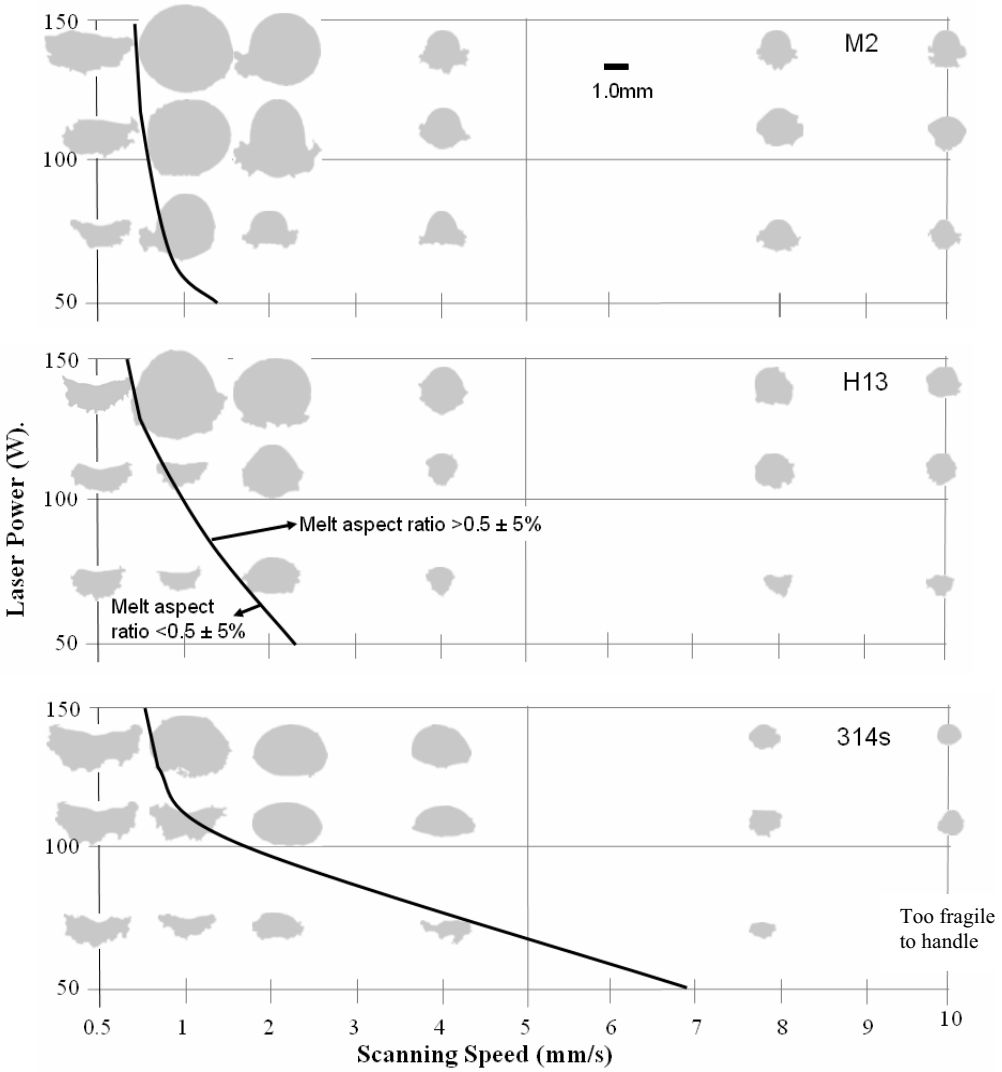

Figure 3. Track cross-sections for M2, H13 and 314S powders, beam diameter 1.1 mm.

Track masses per unit length. Figure 3 clearly shows increase of track cross-section with increase of scan speed at the boundary between flattened and rounded tracks. But the exact areas vary from place to place along a track. To obtain an average measure of size, tracks were removed from their powder beds and weighed. Figure 4 plots mass per unit length against speed for all three powders, for P = 77W. The two regimes, low speed (LS) and high speed (HS), are clear.

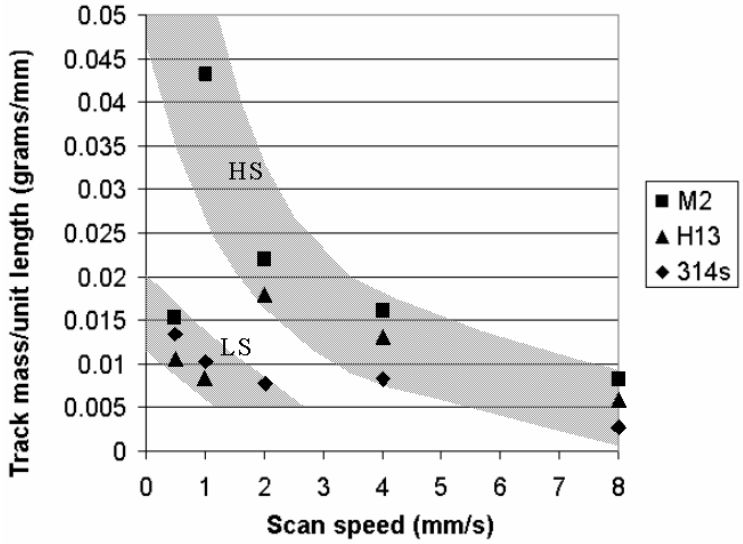

Figure 4. Mass per unit length dependence on scan speed, P = 77W, beam diameter 1.1 mm.

Figure 5 presents an alternative view, plotting mass per unit length against energy density (P/U), for two of the powders (as examples), but for all powers and speeds. In each case, data fall between upper and lower limits. All data for U > 4 mm/s fall on the upper limit, labelled HS. The lower limit labelled LS corresponds to U = 0.5 mm/s. The HS and LS slopes for all materials, and experiments with both laser beam widths, are collected in Table 2, in units of milligram/J. According to equation 2, a constant slope $m_L/(P/U)$ corresponds to a constant 'effective' absorptivity, α^*, obtained from the equality of equation 2. Table 3 gives approximate values of α^* derived from Table 2 on the basis that $C_{av.}$ = 700 J/kg and L = 280 kJ/kg - but see the next section for a more detailed consideration of absorptivity. The HS limits vary with beam diameter.

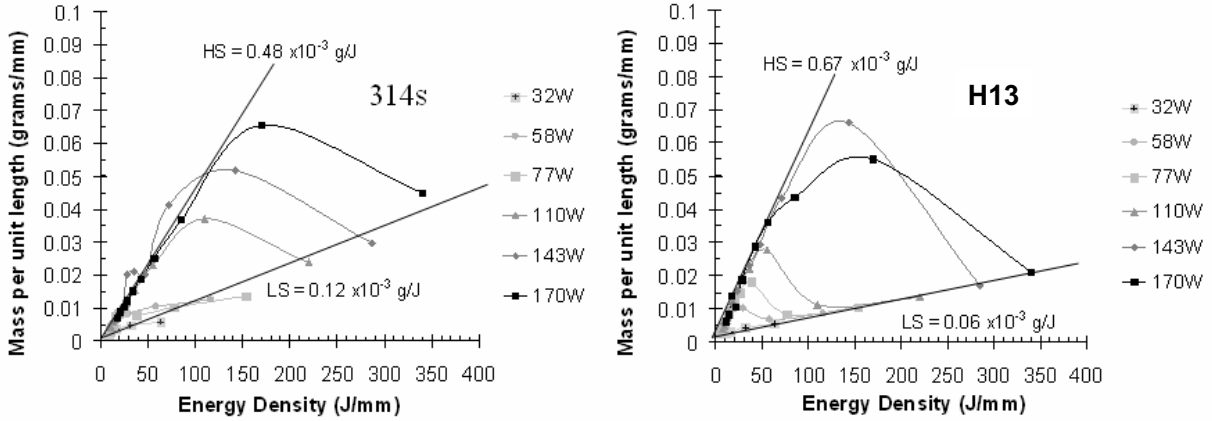

Figure 5: Mass per unit length of 314S and H13 single tracks plotted against energy density for a 1.1mm beam width for 32 < P(W) < 170 and 0.5 < U(mm/s) < 12.

Table 2: Boundary gradients calculated from mass/length vs. P/U figures.

Beam Diameter (mm)	M2 (mg/J)		H13 (mg/J)		314S (mg/J)	
	HS	LS	HS	LS	HS	LS
1.1	0.76	0.10	0.67	0.06	0.48	0.11
0.6	0.84	0.43	-	-	0.59	0.07

Table 3: Values of α^* (Equation 2) calculated from data in Table 2.

Beam Diameter (mm)	M2		H13		314S	
	HS	LS	HS	LS	HS	LS
1.1	0.92	0.12	0.8	0.07	0.58	0.13
0.6	1.0	0.52	-	-	0.79	0.09

Simulations. The main material data used in the simulations is given in Table 4. T_S and T_L are the solidus and liquidus temperatures. Two values of α were used: α_1 from the powder bed temperature distribution thermocouple measurements and α_2 from the HS limit, Table 3, except that for M2 and H13, α_2 was rounded up to 1.0.

Table 4. Material property data used in the simulations.

Mat-erial	K_o (W/mK)	K_v (W/mK^2)	C_o (J/kg)	C_v (J/kgK)	L (kJ/kg)	T_S (°C)	T_L (°C)	ρ_{bed} (kg/m^3)	K_p (W.mK)	α_1	α_2
M2	18.1	0.0106	313	0.5	270	1246	1437	4300	0.26	0.38	1.0
H13	28.6	0.0	313	0.5	270	1361	1471	4500	0.32	0.25	1.0
314S	7.83	0.0183	437	0.275	280	1280	1380	4500	0.26	0.24	0.58

Figure 6 shows a typical simulation result, a boat-shaped track with a crescent cross-section, the consequence of the model allowing only movement of powder material normal to the bed surface on solidification.

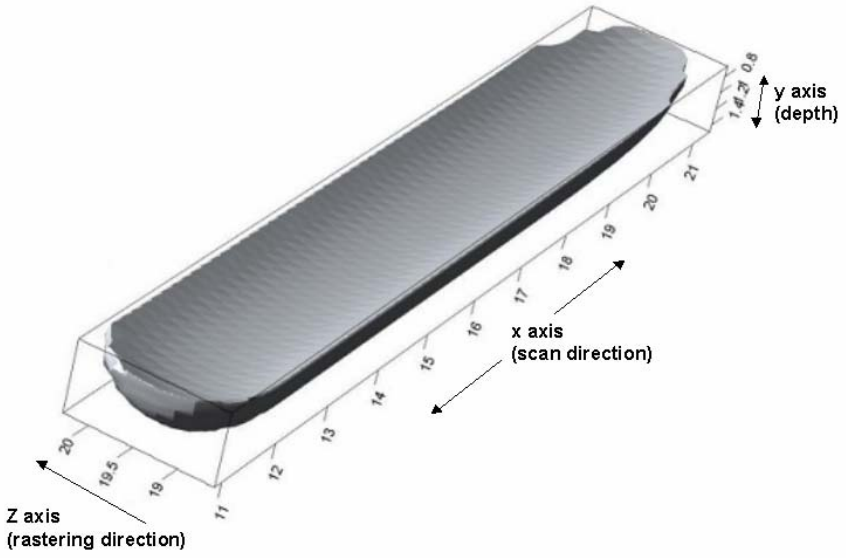

Figure 6. Simulated melt track: P = 100W, U = 6 mm/s, α = 1; dimensions in mm.

Cross-section areas from the simulations were converted to track mass per unit length by multiplying by a solid density of 7,850 kg/m^3. For this purpose, track area was defined as that within the simulated density boundary contour of 7,500 kg/m^3. Table 5 summarises results for P = 77 W in the form of $m_L/(P/U)$, for comparison with the observations of Figure 5 / Table 2. The italic and bold entries are data obtained respectively by use of α_1 and α_2 in the simulations, to be compared with the LS and HS boundary values in Table 2. The simulations follow the same qualitative characteristic as the experiments. However, in the LS range, the data (with the exception of that for M2) range from 0.06 to 0.08, compared to 0.07 to 0.13 in Table 2: for H13, the simulation values are 6% higher than experiments; for 314S they are 36% lower. In the HS range, the data are approximately constant for each material, in line with experiment: comparing Tables 5 and 2, the simulation data are 63 ± 5 % of the experimental ones, for all three materials.

Table 5. $m_{L,simulated}$ / (P/U) (mg/J) - P = 77W, beam diameter = 1.1 mm.

Material	U (mm/s)				
	0.5	1.0	2.0	4.0	8.0
M2	*0.15*	**0.47**	**0.51**	**0.48**	**0.48**
H13	*0.07*	*0.08*	**0.48**	**0.46**	**0.41**
314S	*0.06*	*0.07*	*0.08*	**0.28**	**0.27**

Alternatively, simulated results may be compared to the equivalent point experimental data in Figure 4. Table 6 records the ratio of the simulated to experimental values of mass per unit length. The italicised and bold scripts are obtained with α_1 and α_2, as in Table 5.

Table 6. ($m_{L,simulated}$ / $m_{L,experiment}$), P = 77W, beam diameter = 1.1 mm.

Material	U (mm/s)				
	0.5	1.0	2.0	4.0	8.0
M2	*1.54*	**0.83**	**0.89**	**0.58**	**0.57**
H13	*1.03*	*0.71*	**1.03**	**0.68**	**0.66**
314S	*0.66*	*0.53*	*0.37*	**0.64**	**0.89**

The simulations and experiments differ from each other at both the LS and HS extremes, but in different ways. In the LS conditions, some simulations under- and others over-estimate the experimental observations, although on average they underestimate, and the more so the higher the scan speed. It is probable that the main issue here is uncertainty in what are correct material data to enter into the simulation, particularly the value of α_1. In HS conditions, however, the simulations consistently predict track mass per unit length of around 65% of the observed values. This is despite, for the tool steels, absorptivity of 1.0 being assumed.

There are two possible explanation. The tracks may contain a substantial amount (about one third of their mass) of unmelted powder, e.g. attached round their perimeters. Evidence to support this possibility comes from two directions: a) the simulated track masses reported here on the basis of the track boundary being the 7,500 kg/m^3 boundary contour may be increased by c. 35% by expanding that boundary to include everywhere where any densification at all occurs; b) the experimental observations (Figure 3) frequently show irregular 'skirts' at the track bases (e.g. P = 77W, U = 2 to 10 mm/s for M2). Figure 7 is an enlarged view of the 4 mm/s track section. It shows the skirt occupying c. 30% of the track area. This is typical.

Or the model's assumption of heat transfer normal to the surface only by conduction is wrong. Associated with movements in the bed leading to cylindrical tracks, there may be powder motions that lead to more rapid movement of the melt front into the bed than by conduction. Powder movements are considered more next. Whether an absorption of 1.0 is realistic for CO_2 laser radiation incident on to a steel powder bed is also addressed.

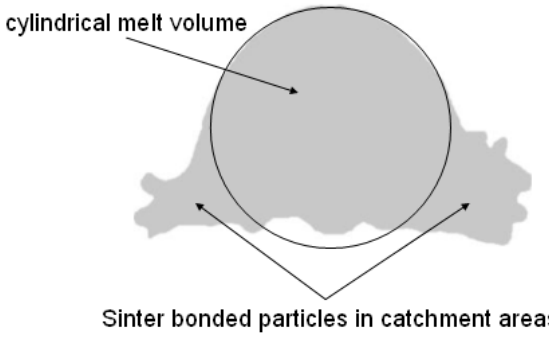

Figure 7. M2 track cross-section enlarged from Figure 3, P = 77W, U = 4 mm/s.

Track photography. Viewing rounded track formation by eye, through the viewing window (Figure 1), revealed periodic melting of powder ahead of the main track. This has been recorded by video-filming through a MIG welding glass filter (actual tracks were bright orange, almost white, directly under the laser beam; without a filter clear images could not be obtained). Figure 8 is an example from filming a M2 track (P = 100 W, U = 1 mm/s).

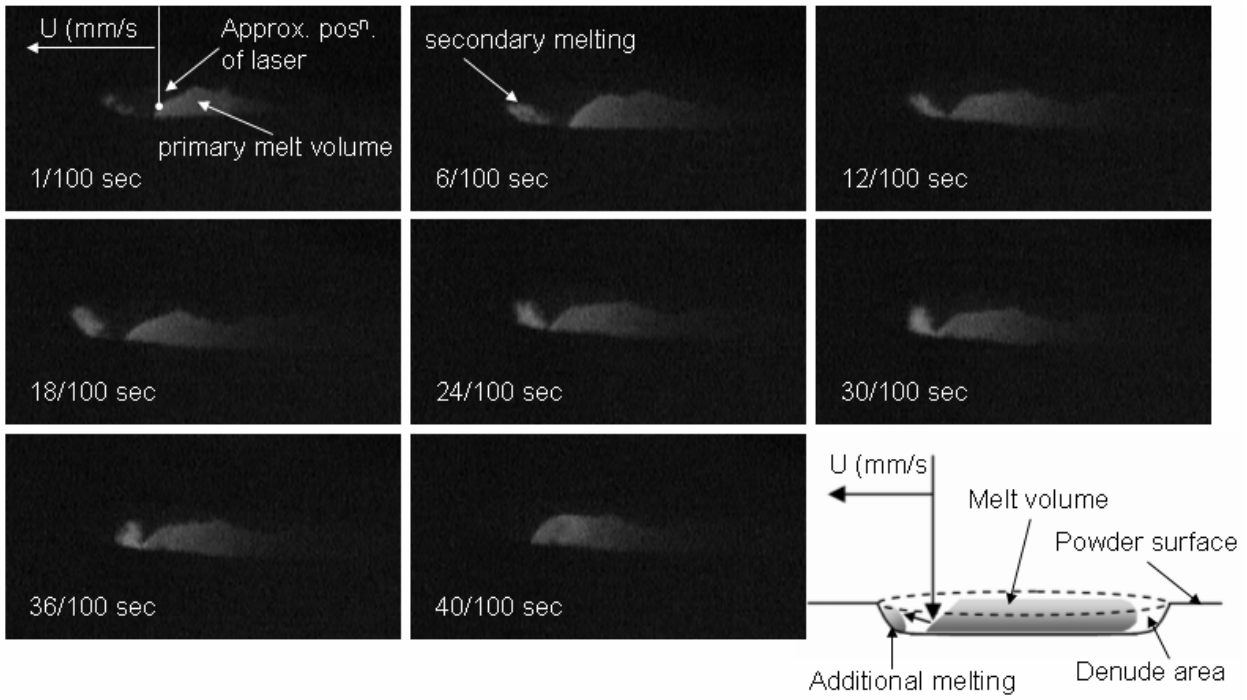

Figure 8. Video stills from track filming for M2: P = 110W, U = 1 mm/s, beam diameter 1.1 mm.

The first frame, at 0.01s, has marked on it the position of the axis of the incident laser beam, judged by where the melted track was brightest. 0.05s later, melting (marked 'secondary melting') is seen ahead of the track. This grows over the next 0.3s and finally flips (too fast to catch on film) into contact with the main track. The process starts again. In summary, tracks do not grow in length steadily but as a series of steps. In this example, the periodic time is about 0.4s. This behaviour is seen qualitatively with all rounded tracks up to a scan speed of 4 mm/s, though filming has been only at 1 mm/s. As speed increases it becomes more difficult to resolve what is happening. A possible explanation of what is happening is illustrated by the sketch in the bottom right corner of Figure 8. Because the melt track is below the powder bed surface and has a steeply sloping nose, it is possible for the incident laser beam to be partly reflected from it on to the end wall of the powder trench in which the track sits. This double absorption opportunity will certainly lead to an increased α, but whether up to 1.0 is not clear.

Single layer formation. Single layers have been created, based on understanding from the single track experiments. Two examples are discussed here (Figure 9), of M2 with P = 110W and U from 0.5 to 8 mm/s, at various scan spacings; and of H13 at P = 110W and U = 4 mm/s. First,

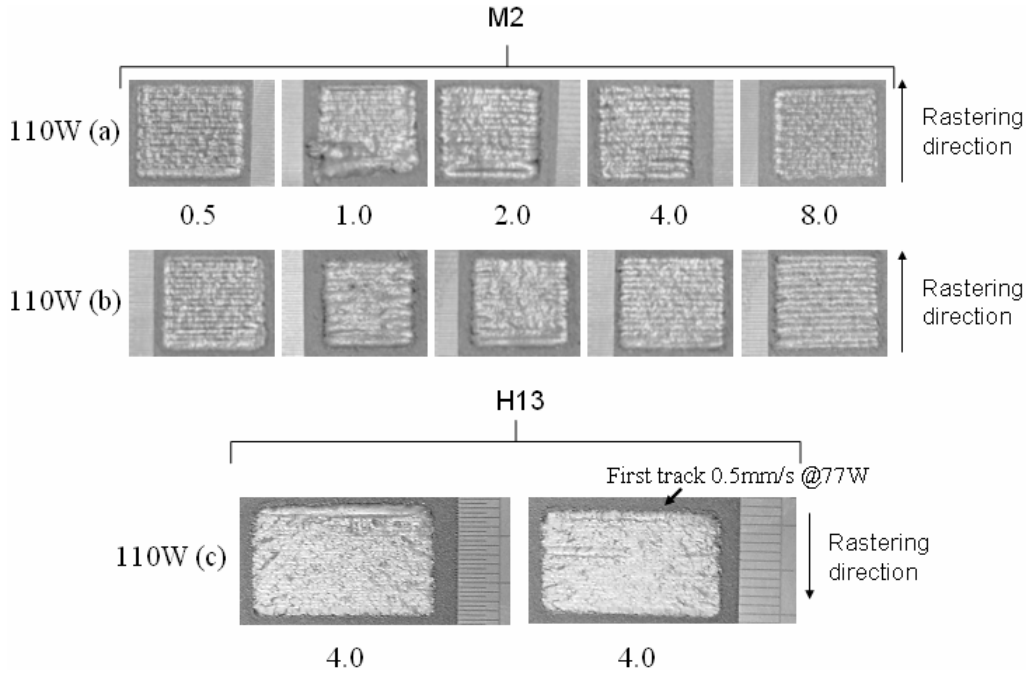

Figure 9. Single layers, with scan spacing as a % of beam diameter; (a) 50%, (b) 100%, (c) 25%.

the surface morphology of layers produced using M2 powder changed from flat to undulating and globular at the (P, U) condition where single tracks changed from flattened to rounded (Figure 3). Improvements in layer quality occurred with a scan spacing of 25% at higher speeds (8.0mm/s), but at lower speeds (1.0-2.0mm/s) the first two/three scan tracks within the layer were often globular and irregular. At a scan spacing of 100%, layers produced at 8mm/s had an undulating surface morphology and the fusion bond between tracks was usually weak, causing areas of porosity. If a scan spacing, as a percentage of single track width is considered instead of as a % of beam diameter, globular layers occur at values lower that ~30% (as in the case for Figure 9a; 1-4mm/s and b, 2mm/s) and undulating and low porosity layers occur at values greater

than ~60%. Layers with improved surface quality shown in Figure 9a, 8mm/s and b, 4mm/s have a scan spacing relative to the melt track width of 40% and 36% respectively. The only exception to this rule occurred in layers produced from flattened tracks (0.5mm/s) where surface quality had less dependence on scan spacing.

Figure 9c makes a different point. Its general condition (P = 110W, U = 4 mm/s) is in the rounded single track regime (Figure 3). The left panel shows the first track indeed to be rounded, but subsequent ones are not. Rounding of tracks is suppressed in layer formation with H13 powder more so than with M2 powder. How pre-existing tracks modify the absorptivity and heat capacity / conductivity environment of a currently melted track is currently under investigation. As a practical point, modifying the first scan power and speed (right panel of Figure 9c) to produce a flattened track at the start of each layer can improve the overall layer morphology.

SUMMARY AND CONCLUSION

Observations of the formation mainly of single tracks, but also layers, of three different steels (M2, H13, 314S) in deep powder beds are reported. In the absence of a constraining solid substrate, tracks may form with a flattened section, a rounded section that sinks into the bed or as broken or balled segments. The different laser power / scan speed conditions in which these occur are mapped and are similar for all three steels. A common observation is that there exists a scan speed range where melted mass increases with increased scan speed. This is not expected from constant power heating models. The speed range is the same as that in which single tracks change from a flattened to a rounded section with increasing speed. Track masses per unit length predicted by a thermal finite element model are in good agreement with experiment when flattened tracks are formed, using thermal absorption coefficients obtained independently, from measurements of temperature / time variations beneath a powder bed surface. To gain agreement when rounded tracks are formed, absorption coefficients close to 1.0 are required. This has led to the video-filming of track formation that has revealed that rounded tracks do not form in a steady manner, but in a way that can enhance laser power absorption, whether up to 100% is another question. Another factor that leads to more track mass than is calculated - from the assumption that all of a track is melted matter - is the possible inclusion of unmelted or partially melted material round the bottom of a track.

A remaining question to be answered is what causes the change from a flattened to a rounded track cross-section. Even without answering it, observations of single track quality can be used to plan the processing conditions for single layers. Here differences of detail occur between one tool steel and another (M2 and H13) with respect to the influence of laser power and scan speed on whether flattened or rounded multi-tracks are formed.

ACKNOWLEDGEMENT

This work was carried out at the University of Leeds as part of a UK EPSRC funded project, ref. no. GR/R32239, linked to two other projects at the Universities of Bradford and Liverpool.

REFERENCES

[1] M. Wohlert, S. Das, J. J. Beaman, D. L. Bourell (1999). Direct laser fabrication of high performance metal components via SLS/HIP. *Proc.10th Solid Freeform Fabrication Symposium*, University of Texas, Austin, pp. 281-288.

[2] W. Meiners, C. Over, K. Wissenbach, R. Poprawe (1999). Direct generation of metal parts and tools by Selective Laser Powder Remelting (SLPR). *Proc.10th Solid Freeform Fabrication Symposium*, University of Texas, Austin, pp. 655-661.

[3] R. H. Morgan, A. J. Papworth, C. Sutcliffe, P. Fox, W. O'Neill (2000). *J Materials Science*, No. 37, pp. 3093-3100.

[4] C. Hauser (2003). Selective laser Sintering of a Stainless Steel Powder, PhD Thesis, University of Leeds.

[5] H. J. Niu, I.T. H. Chang (2000). Selective laser sintering of gas atomised M2 high speed steel powder. *J Materials Science*, No. 35, pp. 31-38.

[6] M. M. A. Dewider, (2002). Direct and Indirect Laser Sintering of Metals, PhD Thesis, University of Leeds.

[7] S. Akhtar, C. S. Wright, M. Youseffi et. al. (2003). Direct Selective Laser Sintering of Tool Steel Powders to High Density. Part B: The Effect on Microstructural Evolution. *Proc.14th Solid Freeform Fabrication Symposium*, University of Texas, Austin.

[8] T. H. C. Childs, M. Berzins, G. R. Ryder, A. Tontowi (1999). Selective laser sintering of an amorphous polymer - simulations and experiments. *Proc. I. Mech. E.* 213B, 333-349.

[9] T. H. C. Childs, A. E. Tontowi (2001). Selective laser sintering of a crystalline and a glass-filled crystalline polymer: experiments and simulations. *Proc. I.Mech.E.* 215B, 1481-1495.

[10] C. M. Taylor, T. H. C. Childs (2002). Morphology of Direct SLS-processed stainless steel layers. *Proc.13th Solid Freeform Fabrication Symposium*, University of Texas, Austin.

[11] S. S. Sih, J. W. Barlow (1992). The measurement of the thermal properties and absorbtances of powders near their melting temperatures. *Proc.3rd Solid Freeform Fabrication Symposium*, University of Texas, Austin, pp. 131-140.

[12] C. Hauser, T. H. C. Childs, K. W. Dalgarno, R. B. Eane (1999). Atmospheric control during direct selective laser sintering of stainless steel 314S powder. *Proc.10th Solid Freeform Fabrication Symposium*, University of Texas, Austin.